Estimating Forces Along Continuum Robots

Vincent Aloi, Khoa T. Dang *Student Member, IEEE*,
Eric J. Barth *Member, IEEE*, and Caleb Rucker *Senior Member, IEEE*

***Abstract*—Continuum robots can be slender and flexible to navigate through complex environments, such as passageways in the human body. In order to control the forces that continuum robots apply during navigation and manipulation, we would like to detect the location, direction, and magnitude of contact forces distributions as they arise. In this paper, we present a model-based framework for sensing distributed loads along continuum robots. Using sensed positions along the robot, we use a nonlinear optimization algorithm to estimate the loading which fits the model-predicted robot shape to the data. We propose that Gaussian load distributions provide a seamless way to account for a wide range of loadings, including approximate point loads and uniform distributed loads, while avoiding the ill-conditioning associated with highly resolved force distributions. In addition, we gain computational efficiency by re-framing the problem as unconstrained weighted least-squares minimization and by solving this problem with an Extended Kalman-filter framework. We validate the approach on two prototype tendon-driven continuum robots in multiple 3D loading scenarios, displaying a mean error of 0.58 N in load magnitude and 7% mean error in load location with respect to the length of the respective robot.**

I. Introduction

Because continuum robots are inherently compliant, their configuration is a function of both actuation and external loading. This poses challenges for control and safety during operation. Sensing environmental interactions is a nontrivial task, since on-board force sensors add weight, give limited information, and may be too large for small-scale surgical robots [1]. This has motivated the use of force estimation methods that rely on sensing secondary information from which the force can be inferred from a model of the robot, effectively using the robot itself as a force sensor. As an example, sensing the actuation forces can provide information about loading at the tip of the robot [2]–[4]. It has also been found that measuring the deflections [5]–[8] or robot curvatures [1], [9], [10] can provide a similar estimate of the tip wrench, or of wrenches at pre-identified points of contact [11]. Bajo et al explored using kinematic information from the robot's motion to determine contact locations [12], [13], and Della Santina used a machine learning algorithm to train a dynamic state observer [14] to detect contact locations. Shape data has been collected from a variety of sources including electromagnetic trackers [7], [15], computer vision [1], [16]–[18], or fiber-Bragg grating sensors [9], [19].

Recent research has made progress on extending force estimation methods to sense general load distributions applied anywhere on a robot's surface. For non-slender soft robots, full 3D elasticity models can be used, which have an associated linearized stiffness matrix. The inverse problem then maps from nodal deflections to loads at each node [16], [17]. However, this approach would be inefficient and highly ill-conditioned for slender continuum robots because their models are typically nonlinear and have high axial stiffness.

A shape-based force estimation problem on slender elastic rods was formulated in [18], in which we used a constrained nonlinear optimization framework to fit a Cosserat rod model to measured shape data by simultaneously selecting the parameters of a force distribution while solving the underlying boundary value problem. Those force distribution parameterizations included Fourier series and Dirac delta functions (point loads) with parameterized locations and magnitudes, normal to the robot surface. A similar framework and loading parameterization was implemented in [20], [21] to sense a number of point forces on a passive medical instrument using an Extended Kalman Filter. [22] also compared direct force computations based on curvature segmentation to estimations of point forces with an unscented Kalman filter.

In this paper we make several important advances upon our prior work [18] and the related work above: (1) we formulate and test our method on *actuated* soft and continuum robots whereas the previous work was applied only to passive rods, (2) we propose an advantageous parameterization of force using Gaussians to efficiently capture the spectrum from point loads to uniform distributed loads without incurring the ill-conditioning seen with highly oscillatory loads, and (3) we improve algorithm efficiency by formulating the estimation as the solution to an unconstrained optimization problem using a penalty method and solving it efficiently with the Extended Kalman Filter framework.

II. Force Estimation Approach

In this section we provide a general force estimation approach for slender continuum robots, where the aspect ratio (length/diameter) of the deforming elastic material (e.g. the backbone) is much greater than 1, usually higher than 5 or 10, such that bending is the dominant mode of the deformation. Given a kinetostatic model (a quasi-static kinematics model that accounts for deformations due to external loads [23]), the approach is capable of estimating multiple point contacts and distributed loads applied at arbitrary locations along the length of the robot.

Manuscript received: February 14, 2022; Revised: May 16, 2022; Accepted: June 7, 2022. This paper was recommended for publication by Editor Cecilia Laschi upon evaluation of the Associate Editor and Reviewers' comments

V. Aloi, K.T. Dang, and C. Rucker are with The University of Tennessee, Knoxville, Department of Mechanical, Aerospace, and Biomedical Engineering, E.J. Barth is with Vanderbilt University, Department of Mechanical Engineering. Parts of this work are based upon work supported by the National Science Foundation under EFMA-1935278 and under IIS-1652588. Any opinion, findings, and conclusions or recommendations expressed herein are those of the author and do not necessarily reflect the views of the National Science Foundation.

Digital Object Identifier (DOI): see top of this page.

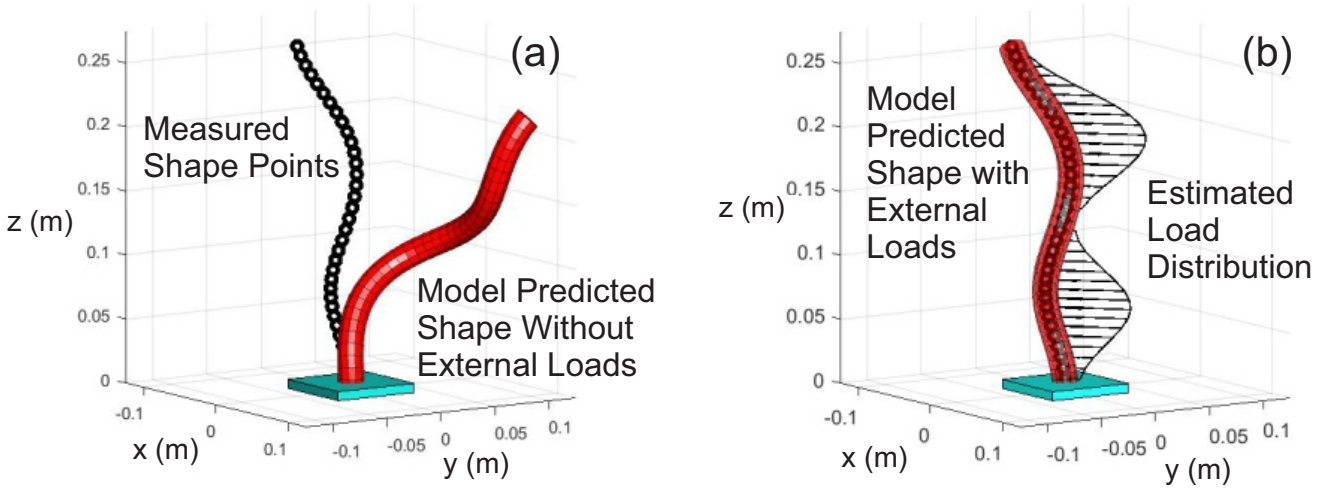

Figure 1. Our approach to the force estimation problem: (a) The model predicted robot shape (after actuation) does not match the measured robot shape due to unmodeled external loads. (b) A distributed load is found that drives the robot model to match the measured shape data.

A. Problem Statement

Using a sensor, the positions of a number of points N_p along a continuum robot are collected. Each point is notated $\boldsymbol{p}_i \in \mathbb{R}^3$ and is located at arc length s_i. We assume a forward kinetostatic model for the robot is known which maps external loading and actuator values to robot shape.

Using a nonlinear optimization approach, a distributed loading can be found which finds the weighted least squares fit between model predicted shape and sensed shape as shown in Figure 1:

$$\begin{aligned} &\underset{\boldsymbol{x}}{\text{minimize}} \quad \tilde{\boldsymbol{z}}^\top \boldsymbol{W} \tilde{\boldsymbol{z}} \\ &\tilde{\boldsymbol{z}}(\boldsymbol{x}) = \hat{\boldsymbol{z}}(\boldsymbol{x}) - \boldsymbol{z} = \begin{bmatrix} \hat{\boldsymbol{p}}_0(\boldsymbol{x}) - \boldsymbol{p}_0 \\ \vdots \\ \hat{\boldsymbol{p}}_{N_p}(\boldsymbol{x}) - \boldsymbol{p}_{N_p} \end{bmatrix} \end{aligned} \tag{1}$$

where $\boldsymbol{x}$ contains unknown inputs to the model such as parameters for external loading, $\tilde{}$ indicates an error between estimated and sensed/known values, $\hat{}$ indicates an estimated value, and $\hat{\boldsymbol{p}}_i(\boldsymbol{x})$ is the 3d coordinate produced by the kinetostatic model given the estimated distributed load. In the vector of unknown inputs, it is often convenient to include parameters which encode a rigid transformation applied to the entire model, such that the optimization simultaneously estimates the loads and performs rigid registration from "measurement space" to "model space". This helps minimize errors from initial registration which can manifest estimations of large forces towards the base of the robot. If $\boldsymbol{\zeta}$ is the twist vector that parameterizes the registration transformation, and $\boldsymbol{\gamma}$ is a vector of paramaters that encode the loading, the vector of unknowns is

$$\boldsymbol{x} = \begin{bmatrix} \boldsymbol{\gamma}^\top & \boldsymbol{\zeta}^\top \end{bmatrix}^\top \tag{2}$$

1) Incorporating Boundary Conditions: Forward kinetostatic models are commonly formulated as boundary value problems where the distal boundary conditions are enforced via a shooting method which applies an optimization routine to the associated initial value problem [4], [5], [24]. In the context of force estimation, it is efficient to combine this model optimization loop with the estimation optimization loop to form a single problem by weakly enforcing the boundary conditions of the kinetostatic through penalty terms added to the objective function of the estimation problem. The weighted least squares framework handles this seamlessly by augmenting the unknown $\boldsymbol{x}$ with $\boldsymbol{\alpha}$, the vector of unknown initial conditions to be solved as $\boldsymbol{x} = \begin{bmatrix} \boldsymbol{\gamma}^\top & \boldsymbol{\zeta}^\top & \boldsymbol{\alpha}^\top \end{bmatrix}^\top$, and augmenting the vector $\hat{\boldsymbol{z}}$ with the vector of distal boundary condition residuals $\boldsymbol{c}(\boldsymbol{x})$ so that the problem is written

$$\begin{aligned} &\underset{\mathbf{x}}{\text{minimize}} \quad \tilde{\boldsymbol{z}}^\top \boldsymbol{W} \tilde{\boldsymbol{z}} \\ &\text{where} \\ &\hat{\boldsymbol{z}} = \begin{bmatrix} \hat{\boldsymbol{p}}_0(\boldsymbol{x}) \\ \vdots \\ \hat{\boldsymbol{p}}_{N_p}(\boldsymbol{x}) \\ \boldsymbol{c}(\boldsymbol{x}) \end{bmatrix} = \boldsymbol{h}(\boldsymbol{x}) \qquad \tilde{\boldsymbol{z}}(\boldsymbol{x}) = \begin{bmatrix} \hat{\boldsymbol{p}}_0(\boldsymbol{x}) - \boldsymbol{p}_0 \\ \vdots \\ \hat{\boldsymbol{p}}_{N_p}(\boldsymbol{x}) - \boldsymbol{p}_{N_p} \\ \\ \boldsymbol{c}(\boldsymbol{x}) \end{bmatrix} \end{aligned} \tag{3}$$

where $\boldsymbol{h}(\boldsymbol{x})$ represents the the nonlinear initial value problem. Choosing the weights of $\boldsymbol{W}$ to be sufficiently high for the boundary conditions can enforce them to within an acceptable tolerance while allowing for the algorithm to converge quickly and stably.

2) Weighted Least Squares with an Extended Kalaman Filter: With a chosen loading parameterization and given kinetostatic model represented by a set of differential equations with boundary conditions, we can solve the weighted least squares problem posed in (3). We propose to use an Extended Kalaman Filter where the data is invariant in time:

$$\begin{aligned} \bar{\boldsymbol{\Sigma}}_i &= \boldsymbol{\Sigma}_i + \boldsymbol{Q} \\ \boldsymbol{K}_i &= \bar{\boldsymbol{\Sigma}}_{i-1} \boldsymbol{H}_i^\top (\boldsymbol{H}_i \bar{\boldsymbol{\Sigma}}_i \boldsymbol{H}_i^\top + \boldsymbol{W}^{-1})^{-1} \\ \boldsymbol{x}_{i+1} &= \boldsymbol{x}_i + \boldsymbol{K}_i \tilde{\boldsymbol{z}} \\ \boldsymbol{\Sigma}_{i+1} &= (\boldsymbol{I} - \boldsymbol{K}_i \boldsymbol{H}_i) \bar{\boldsymbol{\Sigma}}_i \end{aligned} \tag{4}$$

where $\boldsymbol{I}$ is the identity matrix, $\boldsymbol{\Sigma}$ is the co-variance matrix of $\boldsymbol{x}$, $\boldsymbol{Q}$ is conventionally the matrix of expected process noise,

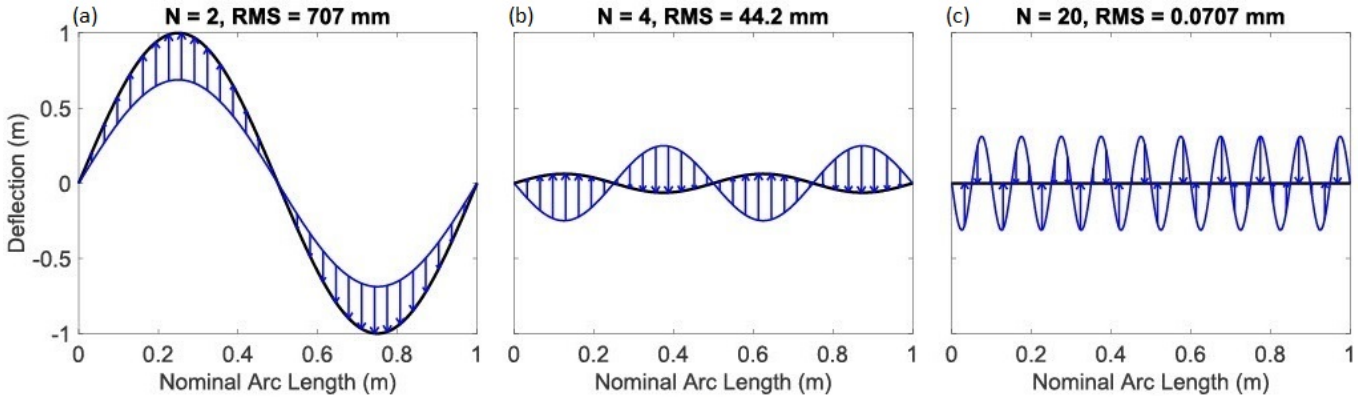

Figure 2. This figure illustrates the ill conditioned nature of the force estimation problem by considering highly oscillatory loads. As the frequency of a sinusoidal distributed load is increased, the resultant deformation of a beam decreases. The beam in this example is $1m$ in length and has a flexural rigidity of $1\,\text{N-m}^2$. The load is a harmonic sinusoid with a constant amplitude of $A = 16\pi^4 \frac{N}{m}$ and an increasing frequency of $\omega = N\pi \frac{rad}{s}$ as in (a) N=2, (b) N=4, and (c) N=20. Because highly oscillatory loads have a minimal effect on the deformed shape, they are not easily sensed by observing position alone.

and $\boldsymbol{H}$ is the Jacobian of $\hat{\boldsymbol{z}} = \boldsymbol{h}(\boldsymbol{x})$ with respect to $\boldsymbol{x}$. It has been noted by [20], [21] that using a Kalaman Filter produced a significant increase in computational efficiency over a Levenberg-Marqardt solver.

With this method, we have two matrices of tunable parameters: $\boldsymbol{Q}$ and $\boldsymbol{W}$. For a given problem, these values can be tuned by hand. In the context of solving a nonlinear least-squares optimization problem, $\boldsymbol{Q}$ has the effect of increasing the damping, thus slowing the convergence and improving stability. Its elements should be chosen such that each value in $\boldsymbol{x}$ can evolve quickly yet stably. If the algorithm is allowed to run until it reaches a steady state solution, the elements of $\boldsymbol{Q}$ will have no effect on the final estimation.

B. Ill-posedness of the Inverse Problem

It is straightforward to map from distributed loading to deformation using a forward kinetostatic model; however, the inverse problem is often ill-posed. There is a family of disparate force distributions that all produce the same deformed shape within a given tolerance. This basic fact limits the effectiveness of any force estimation approach in practice, due to sensor resolution limitations.

1) Uniqueness: As an analytical example of this problem, consider an Euler-Bernoulli beam subject to a distributed load in the shape of a sine wave. Using the differential equation relating shape and load, we can calculate the deflection and its continuous root mean square (RMS), a metric for total shape change:

$$f(s) = A\sin(\omega s) = \frac{1}{EI}\frac{d^4\delta(s)}{ds^4},$$
$$RMS = \sqrt{\frac{1}{L}\int_0^L \delta(s)^2 ds} = \frac{\sqrt{2}AEI}{2\omega^4}. \tag{5}$$

where $\boldsymbol{f}(s)$ is the load, A is its amplitude, ω is its spatial frequency, s is the position along the beam, L is the total length, EI is the flexural rigidity, and $\delta(s)$ is the deflection of a point. From this we can see that RMS deflection is proportional to load amplitude A, but inversely proportional to ω^4. This effect, graphically represented in Figure 2, implies that there are an infinite number of loadings of *arbitrary magnitude* that still produce a shape change that is less than a given minimum value. This principle holds beyond the case of a straight beam with sinusoidal loading: a large-amplitude sinusoidal load with high spatial frequency can be added to any existing loading on a deformed robot, and the resulting deformation will only change minimally. In practical application, this fact can stall a minimization algorithm or cause convergence to a local solution that differs somewhat from the true loading, especially if the force parameterization is highly resolved in space. And the effect is present even in very simple cases with lower spatial frequency. E.g. in [18], oscillatory distributed loads with low-frequency produced (within a very small error tolerance) the same rod shape as a point load at the tip. This highlights the fundamentally ill-posed nature of the force sensing problem.

2) Uncertainty of the Force Estimation: To further probe the nuances of shape-based force estimation, let us consider sensitivity analysis in the simple case of an Euler-Bernoulli beam subject to a point force of magnitude F at position μ. The resultant deflection at the tip is:

$$\delta(L) = \frac{F(3L\mu^2 - \mu^3)}{6EI}. \tag{6}$$

If the measured tip deflection δ is used to estimate the force magnitude and location, we can directly calculate the sensitivity of the estimation to changes in the deflection data as

$$\frac{\partial F}{\partial \delta} = \frac{6EI}{(3L\mu^2 - \mu^3)} \qquad \frac{\partial \mu}{\partial \delta} = \frac{EI}{F(L\mu - \frac{1}{2}\mu^2)}. \tag{7}$$

In Figure 3, these sensitivities are plotted as a function of force magnitude and location. The plot shows that the magnitude estimation becomes more uncertain as the force approaches the base. Intuitively, this is because forces towards the base result in smaller moments and overall less deflection. The same effect can be seen in the location sensitivity plot. However, the location sensitivity is also inversely proportional to the force

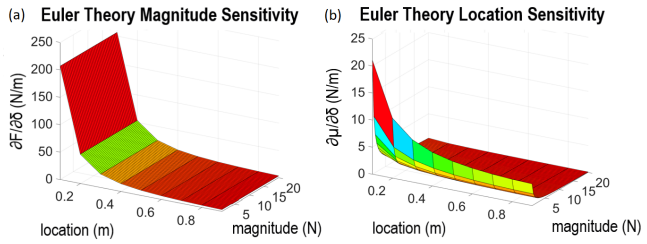

Figure 3. When estimating a force based off of a deflection, (a) the certainty of its magnitude is only related to the point of application. (b) The certainty of its location; however, is a function of both location and magnitude. For this example, a combination of load locations and magnitudes were applied to a beam of length $L = 1m$ with a flexural rigidity of $EI = 1Nm^2$.

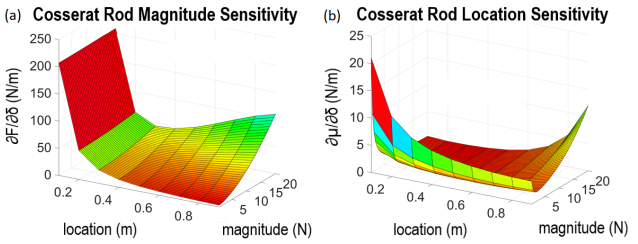

Figure 4. We can see that as forces deflect a cosserat rod into nonlinear deflections, the magnitude (a) and location (b) uncertainties begin to quickly increase as well. In this example, a combination of load locations and magnitudes were applied to a beam of length $L = 1m$ with a flexural rigidity of $EI = 1Nm^2$.

magnitude. Thus, opposed to intuition, forces near the tip are not always more certain than forces at the base.

When using a nonlinear model, such as a Cosserat rod, we can compute these partial derivatives numerically and efficiently using the Jacobian matrix, $\boldsymbol{H}$, from equation (4):

$$\boldsymbol{\gamma} = \begin{bmatrix} F & \mu \end{bmatrix}^\top$$

$$\partial \hat{\boldsymbol{z}} \approx \boldsymbol{H} \partial \boldsymbol{x}$$

$$\begin{bmatrix} \partial \delta \\ \partial \boldsymbol{c} \end{bmatrix} \approx \begin{bmatrix} H_{11} & H_{12} \\ H_{21} & H_{22} \end{bmatrix} \begin{bmatrix} \partial \boldsymbol{\alpha} \\ \partial \boldsymbol{\gamma} \end{bmatrix} \tag{8}$$

$$\begin{bmatrix} \dfrac{\partial F}{\partial \delta} & \dfrac{\partial \mu}{\partial \delta} \end{bmatrix} \approx \left(H_{12} - H_{11} H_{21}^{\dagger} H_{22} \right)^{\dagger}$$

In Figure 4, we see that the sensitivity of the Cosserat Rod agrees with the Euler-Bernoulli sensitivity calculated from 7 in the linear region; however, as the force increases, the sensitivity starts to rise, counter to what the linear theory predicts for both the location and magnitude estimates. Measuring more points along the rod will decrease the uncertainty but it does not remove this fundamental nonlinearity.

C. Loading Parameterization

In order to mitigate the ill-posedness of the problem, we would like to to find a loading parameterization that provides a useful and physically appropriate interpretation of the net loading. The form of the parameterization will be motivated by both the physical construction of the robot and theoretical limitations.

1) Normal Load Assumption: The design of a given manipulator can have a direct effect on what can be sensed using shape data alone. As discussed in [10], for slender robots which have high axial stiffness relative to their bending stiffness, axial strain is minimal and not reliably sensible. As a result, axial components of external loads are difficult to determine from shape data alone. Thus, a major assumption made in this work and related work [18], [21] is that all forces are applied normal to the rod. In many cases, axial forces along the body would only appear through friction which could be assumed to be negligible. Therefore, our distributed load is defined locally:

$$\boldsymbol{f}_{ext}(s) = \boldsymbol{R}(s) \begin{bmatrix} f_{ext}^{x,l}(s) & f_{ext}^{y,l}(s) & 0 \end{bmatrix}^\top, \tag{9}$$

where $\boldsymbol{f}$ is a distributed load, the subscript ext denotes it is an external load, and $\boldsymbol{R}$ maps from local to global coordinates. Given a soft robot with a compressible backbone, it is currently unclear if the shape data would produce unique enough deformations to have reliable sensing; however, initial results from [17] show that an FEA approach can reconstruct a three component force estimation reliably from deflections measured on a soft material.

2) Gaussian Parameterization: As we discussed in II-B above, simply paramaterizing the load with a high-resolution representation (e.g. a Fourier series with many terms, point forces at many locations along the length, or highly resolved splines or polynomials) results in an ill-posed estimation problem because high-frequency oscillatory loads have a minimal effect on shape, as shown in Figure 2. However, such high-frequency oscillatory loads are unlikely to occur in most applications. We expect to commonly encounter point loads and distributed loads that are roughly uniform (e.g. gravity) or have low spatial frequency (e.g. contact with soft tissue on one side). In prior work [18], we explored Fourier series and sliding Dirac-delta functions to parameterize the forces. A conventional Fourier series requires a large number of high-frequency terms to accurately represent point loads, and this led to overfitting and convergence issues on the ill-conditioned problem. Conversely, the Dirac-delta parameterization requires many terms to accurately represent smooth distributed loads, which also leads to over fitting, oscillatory estimation results, and poor convergence. An efficient force parameterization would ideally be able to capture both of these extremes (point loads and smoothly varying distributed loads) in as few terms as possible without introducing the possibility of highly oscillatory force estimations.

We propose that a good candidate for a parameterization that meets these criteria is a series of Gaussian Distribution

Functions:

$$f_{ext}^{x,l} = \sum_{k=0}^{N_l} a_k^x e^{-c_k(s-\mu_k)^2}, \qquad f_{ext}^{y,l} = \sum_{k=0}^{N_l} a_k^y e^{-c_k(s-\mu_k)^2}, \tag{10}$$

where a_k^x and a_k^y are the component amplitudes, μ_k is the mean which encodes the location, and c_k encodes the "steepness" of the function ($c_k \to 0$ approximates a constant load, while $c_k \to \infty$ approximates a point load, and c_k is related to the Gaussian variance σ_k by $2c_k = 1/\sigma_k^2$). A minimum number of load terms, N_l, can be chosen based on the adaptive method from [18], wherein terms are added to the series only when the shape is unable to be fit well by fewer terms. To constrain the location μ_k to be within some reasonable range $\mu_k \in (\beta_1 \quad \beta_2)$ (e.g. the body of the robot, $(0, L)$, or slightly outside) we parameterize it using a sigmoid function:

$$\mu_k = S(\eta_k) = \left(\frac{\beta_2 - \beta_1}{2}\right) \frac{\eta_k}{\sqrt{\epsilon + \eta_k^2}} + \frac{\beta_2 + \beta_1}{2} \tag{11}$$

where ϵ determines the slope of the sigmoid curve, β_1 and β_2 determines the acceptable range of μ_k (it will range from β_1 to β_2), and η_k is the free parameter chosen by the estimation algorithm. We chose this function because it has an upper and lower limit, is monotonic, and has a well defined derivative.

Thus, the set of parameters associated with the Gaussian force distribution is

$$\boldsymbol{\gamma} = [a_1^x \ ... \ a_{N_l}^x, \ a_1^y \ ... \ a_{N_l}^y, \ \eta_1 \ ... \ \eta_{N_l}, \ c_1 \ ... \ c_{N_l}]^\top \tag{12}$$

An added benefit of using Gaussian functions is ease of integration. Integrating the distributed load curve gives the equivalent net load applied at μ_k as:

$$F_k = \sqrt{\frac{\pi}{c_k}} \left\| \begin{bmatrix} a_k^x \\ a_k^y \end{bmatrix} \right\| \tag{13}$$

D. Simulation Study

We verify the benefits of the Gaussian parameterization in two simulation studies. Considering a passive rod of dimensions and material equal to those used in our physical experiments below, we applied loads to the robot model and then estimated those loads based on simulated discrete measurements using our algorithm.

In study 1, we test the reliability of convergence and force estimation accuracy with and without simulated measurement noise. We simulated 100 different cases of a single point load ranging from 0.5 to 1 Newtons, at random locations between 10 cm and 39 cm along the length (the total rod length was 40 cm). Simulated measurements were taken at 20 evenly spaced points along the robot, and we tested the estimation performance using these data with and without added measurement noise (sampled from a normal distribution with zero mean and 1 mm standard deviation). Regardless of the measurement noise, the estimation converged within 500 iterations in greater than 94% of the cases. Without measurement noise, the average error in force location and magnitude was 3.5 mm and 0.08 N respectively. With measurement noise, the errors increased to 20.1 mm and 0.53 N respectively. This confirms that the similar magnitudes of error seen in our physical experiments can be explained by the shape measurement accuracy. Although implemented in Matlab without code optimization, the average time taken per iteration of the algorithm was 23 ms, with 2.1 seconds taken to complete convergence.

In Study 2, we implemented our method using three different parameterizations of the estimated load: the Gaussian parameterization above (using 3 Gaussians, totaling 12 independent parameters), a Fourier series as in [18] (with terms having 0, 1, 2, and 3 periods per robot length, totaling 14 independent parameters), and Dirac delta functions as in [18] (using 4 delta functions, totaling 12 independent parameters). We simulated 100 different cases where the rod was subjected to a general distributed load defined by two 10^{th} degree polynomials in s in the local x and y directions, constrained such that the distributed force was less than 5 N/m everywhere. The Gaussian parameterization converged 99% of the time with an average RMS shape error of 0.66 mm. The dirac delta parameterization converged 93% of the time, with an average RMS shape error of 1.4 mm. The Fourier parameterization converged 92% of the time with an average RMS shape error of 4.1 mm. The Gaussian parameterization shows had the most reliable convergence and resulted in shape fitting errors an order of magnitude smaller than of the Fourier parameterization.

III. Experimental Validation

To validate the proposed force estimation approach, we will apply the methodology to two tendon-actuated continuum robots in 3D (one single DOF and one multi-DOF). These experiments contained significant gravity loading, actuation loading, and both out-of-plane an in-plane external loading. The estimation was performed using sparse data along the rod: only eight points along the robot were measured using a stereoscopic camera system.

A. Tendon Robot Model

We implemented the tendon robot model presented in [25], [26]. The backbone of the robot is treated as a Cosserat rod where the tendons apply a distributed wrench along the length and a tip wrench. The shape of a rod is described by the position of its centerline $\boldsymbol{p}(s) \in \boldsymbol{R}^3$, and a rotation matrix, $\boldsymbol{R}(s) \in$ SO(3), representing its material orientation as a function of arc length $s \in [0 \quad L]$. The derivatives of $\boldsymbol{p}$ and $\boldsymbol{R}$ with respect to s are defined by

$$\mathbf{p}' = \mathbf{R}\mathbf{v}, \qquad \mathbf{R}' = \mathbf{R}\mathbf{u}^\wedge, \tag{14}$$

where the kinematic variables $\mathbf{v}(s)$ and $\mathbf{u}(s)$ are the linear and angular rates of change of a material attached transformation expressed in the local body-frame coordinates. The $\wedge$ operator, as defined in [27], maps $\mathbb{R}^3$ to 3 (the skew-symmetric matrices, the Lie algebra of the Lie group $\mathrm{SO}(3)$).

Performing a static balance on a section of rod and taking a derivative, we can describe the rates of change of the internal force vector $\mathbf{n}(s)$ and the internal moment vector $\mathbf{m}(s)$ with respect to arc length:

$$\begin{aligned} \boldsymbol{n}' &= -(\boldsymbol{f}_{ext} + \boldsymbol{f}_t + \boldsymbol{f}_g) \\ \boldsymbol{m}' &= -(\boldsymbol{p}' \times \mathbf{n} + \boldsymbol{l}_t), \end{aligned} \tag{15}$$

where $\boldsymbol{l}$ a distributed moment, subscript "t" indicates it is a tendon load, and subscript "g" indicates it is a gravitational load. Note, however, that $\boldsymbol{f}_t$ and $\boldsymbol{l}_t$ are nonlinear functions of the state and state derivatives. The resulting ODE's can be written in an explicit form, which is detailed in [25].

The internal force and moment vectors are related to $\mathbf{v}$ and $\mathbf{u}$ via a material constitutive law. Commonly, a linear law is used:

$$\boldsymbol{n} = \boldsymbol{R}\boldsymbol{K}_{se}\left(\boldsymbol{v} - \boldsymbol{v}^*\right), \qquad \boldsymbol{m} = \boldsymbol{R}\boldsymbol{K}_{bt}\left(\boldsymbol{u} - \boldsymbol{u}^*\right) \tag{16}$$

where $\boldsymbol{v}^*$ and $\boldsymbol{u}^*$ are appropriate kinematic variables of the rod in its stress free reference state ($\boldsymbol{u}^* = \mathbf{0}$ and $\boldsymbol{v}^* = [0\ 0\ 1]^\top$ for an initially straight rod), and $\mathbf{K}_{se} = \text{diag}\left(GA, GA, EA\right)$ and $\mathbf{K}_{bt} = \text{diag}\left(EI, EI, GJ\right)$ are stiffness matrices in terms of the rod's cross-sectional area A, Young's modulus E, shear modulus G, area moment of inertia I, and polar moment of inertia J. Combining Equations 14, 15, and 16, we have a system of differential equations that describe the evolution of $\boldsymbol{p}$, $\boldsymbol{R}$, $\boldsymbol{n}$, and $\boldsymbol{m}$ with respect to s.

Given the tension in the tendons, this system can be solved as a boundary value problem using a shooting method. Distal boundary conditions are derived from a static balance at the tip:

$$\boldsymbol{c}(\boldsymbol{x}) = \begin{bmatrix} \boldsymbol{n}(L) - \boldsymbol{F}_t \\ \boldsymbol{m}(L) - \boldsymbol{M}_t \end{bmatrix}, \tag{17}$$

where $\boldsymbol{F}$ and $\boldsymbol{M}$ are the tip forces and moments applied by the tendons. The unknown initial conditions are the base wrench:

$$\boldsymbol{\alpha} = \begin{bmatrix} \boldsymbol{n}(0) \\ \boldsymbol{m}(0) \end{bmatrix}. \tag{18}$$

If a tendon terminates prior to to the tip of the robot, a piecewise integration routine must be used [25].

B. Robotic Setup

For the first set experiments, a robot with a single tendon was constructed, as seen in Figure 5. It consisted of a 1.4 mm diameter backbone, nine PLA spacer disks, and Kevlar thread. The length of the robot was 40cm and the disks were evenly spaced 5 cm apart. The tendon terminated at the final disk and was connected to a load cell. This load cell was affixed to a linear actuator. The tendon was routed parallel to the back bone at a distance of 7 mm. The backbone was made of ASTM A228 Spring steel, which has a nominal Young's modulus of 207 GPa and shear modulus of 79 GPa. Finally, optical markers were attached to the spacer disks so we could record their 3D positions. This provided $N_p = 9$ data points. The robot was oriented such that the tendon would move the end effector in the plane of gravity.

For the second set of experiments, we constructed a multi-segment robot with larger diameter and two tendons as seen in Figure 5. Similar to the one before, we used a spring steel rod backbone and nine spacer disks, evenly spaced at 7 cm apart. However, this robot was significantly larger, with a length of 56 cm. The tendons were routed parallel to the backbone at an offset of 2.5 cm. The tendons were placed on orthogonal sides. The tendon that actuates in the plane of gravity terminates at end effector, and the second tendon terminates at the disk halfway down the robot such that when both tendons are actuated, the robot has two bending segments in different planes.

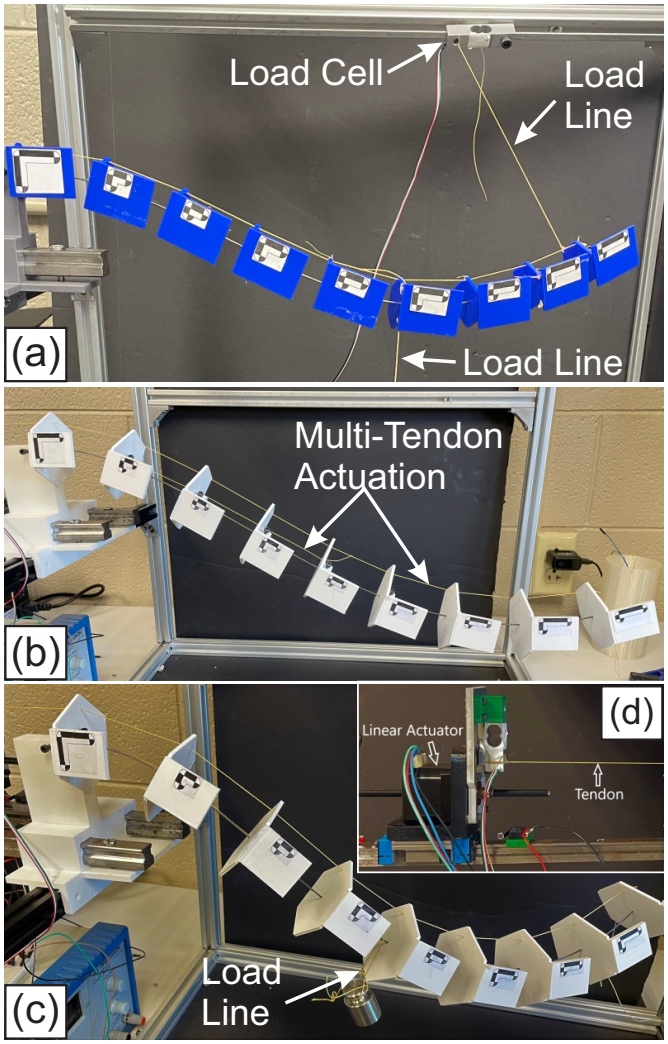

Figure 5. Experiments were performed on a a single-tendon robot (a) and a multi-tendon robot (b & c), made from a spring steel rod plastic disks. As shown in (d), Linear actuators controlled the tendon displacement and each tendon's tension was measured by a load cell. External loads were applied to various points on the robot structure using Kevlar thread. External forces were measured using load cells as in (a) or by applying the load using a calibration weight as in (b) to validate the force estimation algorithm.

C. Calibrating Gravitational Load

It is not necessary to know the gravitational loading a priori. However, if we do include a known gravity loading, the estimation algorithm will separately determine the non-gravitational loads. Thus, we include the gravity loading as

$$\boldsymbol{f}_g = \rho \boldsymbol{a}_g \tag{19}$$

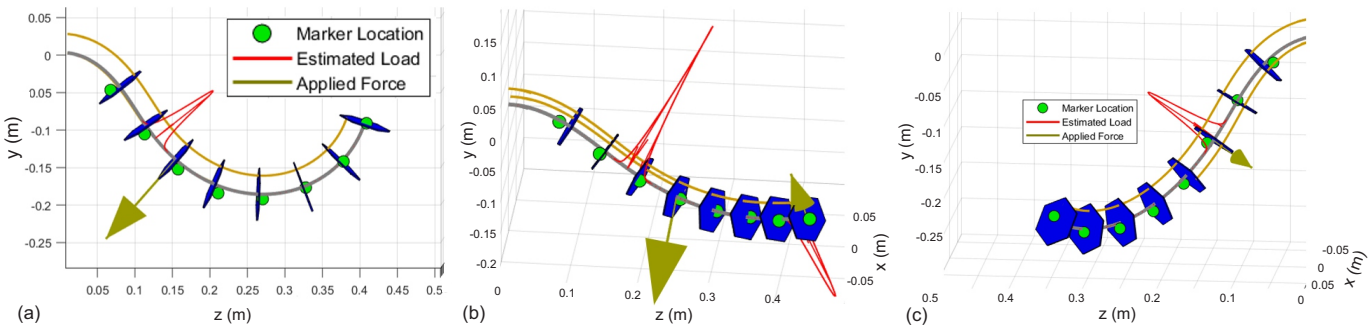

Figure 6. Using a 2 DoF robot, experiments were performed to validate non planar loading and actuation. Above are 3 example cases from the experiment set. Using shape data and known tendon tensions, the algorithm is able to find appropriate forces necessary to recreate that shape. The yellow arrows represent the measured applied forces. The estimated distributed load is drawn in red. Note that their directions are consistent because the red distribution is applied toward the backbone.

Table I
SINGLE LOAD CASES FOR 1 DOF TENDON ROBOT

In Plane				
Actuation (cm)	Magnitude (N)		Location (cm)	
	Meas.	Estimated	Meas.	Estimated
11.5	0.06	0.04	30	25
11.5	1.2	0.7	10	10
5	3.9	4.8	10	7
5	0.5	0.4	30	28
-5	0.7	0.6	10	12
-5	2.5	2.0	10	10
Out of Plane				
11.5	0.6	0.7	30	29
11.5	1.4	2.3	10	8.5
0	4.2	4.2	10	7.7
0	0.7	0.8	30	27

where ρ is the mass per length, and $\boldsymbol{a}_g$ is the gravitational acceleration vector. We calibrated ρ separately before the estimation experiments by using the estimation algorithm assuming the only external load is gravity. The calibrated mass per length was $\rho = 0.144\frac{kg}{m}$ for the 1 DoF Robot and $\rho = 0.252\frac{kg}{m}$ for the 2 DoF Robot.

D. Procedure and Results

For the 1 DoF Robot, a load cell was used to create a single point force both in and out of plane. The loading was placed at varying contact locations and with the robot actuated into various poses. The cables were oriented such that they were normal to the rods backbone. An optical micron tracker was used to capture the shape data. The results are listed in Table I. Actuation values in the table denote the amount the tendon's actuator was displaced from the nominal position (along the positive z-axis). For the estimation, the loading was parameterized as a single Gaussian curve.

The mean magnitude error was 0.32 N and the mean location error was 2.7 cm (7% of total robot length). Even with the extra loading from gravitational forces and actuation, the force magnitude was of same order of accuracy as the experiments performed on a cantilevered rod in [18] (0.29 N). The location error was slightly larger but only by a few percent of the total length (2-3%). Comparing the planar and non planar cases, the difference in accuracy is negligible.

Table II
DOUBLE LOAD CASES FOR 1 DOF TENDON ROBOT

In Plane				
Actuation (cm)	Load Magnitude (N)		Load Location (cm)	
	Measured	Estimated	Measured	Estimated
0	3.3 1.9	3.9 1.4	20 30	15 30
0	5.0 2.9	5.4 2.2	30 20	29 15
-5	2.2 1.6	3.8 1.1	10 30	12 27
-5	9.6 2.5	8.6 3.2	10 30	10 26
Out of Plane				
0	3.2 1.9	3.8 2.4	25 40	24 36
0	1.52 0.72	1.86 0.92	25 40	12 23
-5	5.6 0.9	4.2 0.4	10 35	9 28
-14.5	0.8 0.4	0.9 0.5	40 25	39 22

Next, we used two load cells to apply two point forces both in and out of plane, such as in Figure 5. As before, we tested loads at various locations and different robot poses. These results are given in Table II. For the estimation in these experiments, the loading was parameterized as two gaussian curves. The number of Gaussian curves necessary to solve the estimation problem can be adaptively selected based on the goodness of fit, and the improvement seen by introducing more terms, similar to the methods proposed in [18] and [21]. Even with the robot loaded into large nonlinear deflections, the accuracy remained consistent. There was a mean error of 0.51 N and 2.64 cm for the magnitude and location, respectively.

In the second set of experiments, we actuated the 2 DoF Robot into eight poses with both single and double loading scenarios, as summarized in Table III, where DoF 1 is the longer tendon and DoF 2 is the shorter tendon. We did six

Table III
2 DOF TENDON ROBOT EXPERIMENTS

Actuation (cm)		Load Magnitude (N)		Load Location (cm)	
DoF 1	DoF 2	Measured	Estimated	Measured	Estimated
-25	0	1.17	1.44	14	18.9
-15	-5	1.39	1.58	28	20.6
-30	0	5.21	3.71	21	19.8
-20	-20	1.59	2.68	21	23.5
-30	-5	5.57	3.62	21	20.0
-20	-10	1.01	1.99	21	21.6
-30	-5	2.87	3.02	21	19.4
		0.49	0.60	52	46.0
-10	0	1.96	2.11	35	22.7
		1.09	0.93	55	52.7

single load cases and two double load cases. The overall results were similar to that of the 1 DoF experiments with mean errors of 0.65 N and 3.98 cm (7.2%) in magnitude and location, respectively. This shows that the increased complexity from multi-tendon loading and large non-planar deflections does not limit the estimation accuracy. In Figure 6, we provide a showcase of three examples comparing the model estimation and actual loading.

IV. CONCLUSIONS

We have formulated and validated a method for shape-based estimation of forces along actuated continuum robots in 3D. We explored the ill-posed nature of the estimation problem, revealing that highly oscillatory loads are a main source of the ill-conditioning. Consequently, force parameterizations that require high resolution to represent commonly encountered loads are not ideal. We proposed a nonlinear Gaussian parameterization to represent a large spectrum of loads (from point forces to smooth distributed loads), with a small number of parameters, and advantages were shown in simulation. Experimental validation of the method on two separate tendon-actuated robots resulted in reasonable performance in both magnitude and location accuracy.

REFERENCES

[1] M. Khoshnam, A. C. Skanes, and R. V. Patel, "Modeling and Estimation of Tip Contact Force for Steerable Ablation Catheters," *IEEE Transactions on Biomedical Engineering*, no. 5, pp. 1404–1415, may.

[2] K. Xu and N. Simaan, "An Investigation of the Intrinsic Force Sensing Capabilities of Continuum Robots," *IEEE Transactions on Robotics*, no. 3, pp. 576–587, jun.

[3] L. Lindenroth and C. Duriez, "Intrinsic force sensing capabilities in compliant robots comprising hydraulic actuation Development of a Robotic Trans-esophageal Ultrasound System View project Robotic Ultrasound Systems for Intelligent Fetal Imaging and Diagnosis View project."

[4] C. B. Black, J. Till, and D. C. Rucker, "Parallel Continuum Robots: Modeling, Analysis, and Actuation-Based Force Sensing," *IEEE Transactions on Robotics*, no. 1, pp. 29–47, feb.

[5] D. C. Rucker and R. J. Webster, "Deflection-based force sensing for continuum robots: A probabilistic approach," in *2011 IEEE/RSJ International Conference on Intelligent Robots and Systems*. IEEE, sep, pp. 3764–3769.

[6] J. Back, L. Lindenroth, R. Karim, K. Althoefer, K. Rhode, and H. Liu, "New kinematic multi-section model for catheter contact force estimation and steering," in *2016 IEEE/RSJ International Conference on Intelligent Robots and Systems (IROS)*. IEEE, oct, pp. 2122–2127.

[7] H. Yuan, P. W. Y. Chiu, and Z. Li, "Shape-Reconstruction-Based Force Sensing Method for Continuum Surgical Robots With Large Deformation," *IEEE Robotics and Automation Letters*, no. 4, pp. 1972–1979, oct.

[8] J. Back, L. Lindenroth, K. Rhode, and H. Liu, "Three dimensional force estimation for steerable catheters through bi-point tracking," *Sensors and Actuators A: Physical*, pp. 404–415, aug.

[9] R. Xu, A. Yurkewich, and R. V. Patel, "Curvature, Torsion, and Force Sensing in Continuum Robots Using Helically Wrapped FBG Sensors," *IEEE Robotics and Automation Letters*, no. 2, pp. 1052–1059, jul.

[10] F. Khan, R. J. Roesthuis, and S. Misra, "Force sensing in continuum manipulators using fiber Bragg grating sensors," in *2017 IEEE/RSJ International Conference on Intelligent Robots and Systems (IROS)*. IEEE, sep, pp. 2531–2536.

[11] C. M. Heunis, V. Belfiore, M. Vendittelli, and S. Misra, "Reconstructing Endovascular Catheter Interaction Forces in 3D using Multicore Optical Shape Sensors," in *IEEE International Conference on Intelligent Robots and Systems*. Institute of Electrical and Electronics Engineers Inc., nov 2019, pp. 5419–5425.

[12] A. Bajo and N. Simaan, "Finding lost wrenches: Using continuum robots for contact detection and estimation of contact location," in *2010 IEEE International Conference on Robotics and Automation*. IEEE, may, pp. 3666–3673.

[13] ——, "Kinematics-Based Detection and Localization of Contacts Along Multisegment Continuum Robots," *IEEE Transactions on Robotics*, no. 2, pp. 291–302, apr.

[14] C. D. Santina, R. L. Truby, and D. Rus, "Data–Driven Disturbance Observers for Estimating External Forces on Soft Robots," *IEEE Robotics and Automation Letters*, no. 4, pp. 5717–5724, oct.

[15] S. Song, Z. Li, H. Yu, and H. Ren, "Shape reconstruction for wire-driven flexible robots based on Bézier curve and electromagnetic positioning," *Mechatronics*, pp. 28–35, aug.

[16] Z. Zhang, J. Dequidt, and C. Duriez, "Vision-Based Sensing of External Forces Acting on Soft Robots Using Finite Element Method," *IEEE Robotics and Automation Letters*, vol. 3, no. 3, pp. 1529–1536, jul 2018.

[17] Z. Zhang, A. Petit, J. Dequidt, and C. Duriez, "Calibration and External Force Sensing for Soft Robots Using an RGB-D Camera," *IEEE Robotics and Automation Letters*, vol. 4, no. 3, pp. 2356–2363, jul 2019.

[18] V. A. Aloi and D. C. Rucker, "Estimating loads along elastic rods," in *Proceedings - IEEE International Conference on Robotics and Automation*, vol. 2019-May. Institute of Electrical and Electronics Engineers Inc., may 2019, pp. 2867–2873.

[19] E. Coevoet, A. Escande, and C. Duriez, "Optimization-Based Inverse Model of Soft Robots With Contact Handling," *IEEE Robotics and Automation Letters*, no. 3, pp. 1413–1419, jul.

[20] Q. Qiao, D. Willems, G. Borghesan, M. Ourak, J. De Schutter, and E. V. Poorten, "Estimating and localizing external forces applied on flexible instruments by shape sensing," *2019 19th International Conference on Advanced Robotics, ICAR 2019*, pp. 227–233, dec 2019.

[21] Q. Qiao, G. Borghesan, J. D. Schutter, and E. V. Poorten, "Force from shape–estimating the location and magnitude of the external force on flexible instruments," *IEEE Transactions on Robotics*, 2021.

[22] O. Al-Ahmad, M. Ourak, J. Vlekken, and E. Vander Poorten, "FBG-Based Estimation of External Forces Along Flexible Instrument Bodies," *Frontiers in Robotics and AI*, p. 232, jul.

[23] E. P. Dupont, N. Simaan, H. Choset, and C. Rucker, "Continuum Robots for Medical Interventions," *Proceedings of the IEEE*, 2022.

[24] J. Till, C. E. Bryson, S. Chung, A. Orekhov, and D. C. Rucker, "Efficient computation of multiple coupled Cosserat rod models for real-time simulation and control of parallel continuum manipulators," in *2015 IEEE International Conference on Robotics and Automation (ICRA)*. IEEE, may, pp. 5067–5074.

[25] D. C. Rucker and R. J. Webster III, "Statics and Dynamics of Continuum Robots With General Tendon Routing and External Loading," *IEEE Transactions on Robotics*, no. 6, pp. 1033–1044, dec.

[26] K. Oliver-Butler, J. Till, and C. Rucker, "Continuum Robot Stiffness under External Loads and Prescribed Tendon Displacements," *IEEE Transactions on Robotics*, vol. 35, no. 2, pp. 403–419, apr 2019.

[27] R. M. Murray, Z. Li, and S. Sastry, *A mathematical introduction to robotic manipulation*. CRC Press, 1994.